Chapter 19
Flow Boiling and Two-Phase Flow of CO_2

Summary: An overview of the state-of-the-art of two-phase flow pattern maps, two-phase pressure drops and flow boiling heat transfer of carbon dioxide is described here for internal flows, covering both macrochannels and microchannels without distinction. This chapter addresses experimental studies and prediction methods for CO_2, together with some comparisons of these methods to experimental databases. Because of the specific interest in CO_2 and its unique nature (most conventional refrigerant methods do not work directly for CO_2 when they are extrapolated to significantly higher pressures), these thermal design methods for CO_2 are presented all together here in this chapter.

19.1 Introduction

Carbon dioxide has received significant scientific and industrial interest in the past decade or so as a natural, environmentally safe refrigerant. It is currently being used ever more widely for low temperature refrigeration systems and in heat pumps. CO_2 is also a good selection as a secondary refrigerant for low temperature applications. Considerable efforts have also been made for its application to automotive air-conditioning systems, although its widespread use there is currently in competition with other new possible replacements for R-134a. Due to its low critical temperature of 31.1°C (88°F) and high critical pressure of 73.8 bar (1070 psia) relative to conventional refrigerants, CO_2 systems operate at much higher working pressures. In particular, the higher operating pressures result in much higher reduced pressures, vapor densities and vapor viscosities and much lower surface tensions and liquid viscosities.

As a consequence, flow boiling heat transfer coefficients tend to be much larger for CO_2 than for conventional refrigerants when compared at the same saturation temperature. Primarily this is due to the fact that CO_2 has nucleate boiling heat transfer coefficients that are much larger than those of conventional refrigerants and thus its nucleate boiling contribution is usually much larger than the corresponding convective heat transfer contribution to flow boiling at low vapor qualities, which is not the case for conventional refrigerants. Furthermore, the flow pattern transitions for CO_2 are quite different from those of conventional refrigerants when evaluated at the same saturation temperature. In particular, the onset of dryout and beginning of mist flow tend to occur much earlier for flow boiling of CO_2 in both small and large diameter tubes (i.e. it occurs at lower vapor qualities) and this leads to a much earlier degradation in the flow boiling heat transfer coefficient. Notably, extrapolation of conventional refrigerant design methods to the much higher working pressures of interest for CO_2 does not usually work, and when it happens that a conventional method does predict a set of CO_2 flow boiling data, it seems to be more of a coincidence than a general validation. Clouding the issue, unfortunately, there are a number of experimental studies whose results differ significantly from others at similar test conditions for no specific reason. Thus, as a general recommendation, one should use only CO_2 thermal design methods that have been widely validated for a broad, detailed database comprising results taken at independent laboratories.

Thome and Ribatski (2005) recently reviewed the CO_2 literature, addressing experimental studies on flow boiling heat transfer, two-phase flow pattern observations and two-phase pressure drops measured in macrochannels and microchannels, analogous prediction methods for CO_2 and comparisons of these methods to independent experimental data extracted from the same literature. Due to the lack of a well-established criterion to identify the transition between macroscale and microscale channel sizes, they arbitrarily adopted a diameter of 3 mm to segregate their databases. Regarding nucleate pool boiling of

CO_2, not many experimental results are available. The reader is referred to Gorenflo and Kotthoff (2006) for a review of the limited data available for nucleate pool boiling of CO_2.

This chapter presents the following topics in the following order: (i) two-phase flow pattern observations and CO_2 specific flow pattern maps, (ii) two-phase pressure drop data and prediction methods and (iii) flow boiling heat transfer studies and CO_2 specific flow boiling prediction methods. Some comparisons of the CO_2 methods and some conventional refrigerant methods to independent data sets will also be presented. The present chapter is based primarily on the author's recent work on this topic and hence for more detailed information on any particular aspect, the reader is referred to the Thome and Ribatski (2005) and Cheng et al. (2006, 2007, 2008a, 2008b).

Many tests for CO_2 are for channels with non-circular cross-sections. To reflect the real mass flow velocities, equivalent diameters are used here for predicting flow pattern map transitions, two-phase pressure drops, and heat transfer coefficients of non-circular channels rather than hydraulic diameters. The equivalent diameter is defined as that of a circular cross-section channel with the same area as the non-circular channel. The equivalent diameter is also thus used to calculate void fractions, mean velocities of the phases, etc. Furthermore, in this chapter for determining the nucleate boiling contribution to flow boiling, the heat flux is calculated from the heat duty applied the actual perimeter of the channel. It would actually be best to apply the heat duty to the perimeter of the equivalent diameter, but experimental studies often do not indicate how they have defined their heat flux for non-circular channels (on the actual perimeter or on their quoted hydraulic diameter's perimeter). Hence, we have used the convention here of inputting the heat flux based on the actual perimeter. This value is not normally that different than that based on the equivalent diameter, but is still something to reflect on when reading and writing published papers and implementing prediction methods.

19.2 Two-Phase Flow Patterns and Maps for CO_2

Not too many flow pattern observation studies have been conducted for CO_2, primarily because of the elevated pressures. Several of those available are described here.

Yun, Kim and Kim (2003) and Yun and Kim (2004) investigated two-phase flow regimes of CO_2 in a narrow rectangular horizontal channel of 2 mm by 16 mm (0.079 in. by 0.630 in.). Their test section consisted of a side groove in a stainless steel body with a glass cover as the upper wall of the channel. Cartridge heaters were used to supply heat to the channel, allowing simultaneous flow visualization with a CCD camera during flow boiling measurements. They observed bubbly flow, intermittent flow (sometimes with flat wide bubbles as an elongated bubble flow regime) and annular flow, the latter with some liquid drops entrained in the vapor core that increased in frequency with increasing mass velocity. They noted that at the same saturation temperature, the annular flow transition for CO_2 occurred at a relatively higher vapor quality relative to that for R-22.

Yun and Kim (2003b) in another study carried out two-phase flow boiling experiments to investigate dryout of the liquid film. They tested horizontal stainless steel tubes with diameters of 0.98 and 2.0 mm (0.0386 and 0.079 in.) with direct current heating of the test sections. The critical vapor qualities they obtained (those at the onset of dryout) were detected by a sharp local increase in the tube wall temperature. According to their data, increasing the heat flux reduced the critical quality (that is anticipated the onset of dryout to lower vapor qualities) while increasing the mass velocity slightly increased the critical quality.

In another study by the same group, Yoon et al. (2003, 2004) have proposed a correlation for predicting the dryout vapor quality. Curiously, when trying out their method to predict dryout vapor qualities for the

heat transfer database used by Chen et al. (2006), 68% were predicted to be higher than 1.0. This behavior is due the extrapolation of their correlation to a wider range of the tube diameters (their experimental database included only one tube diameter of 7.53mm (0.296 in.)). Thus, this is a good illustration that one must be careful when applying methods outside of their original range of application.

Using a high-speed digital camera and magnification, Pettersen (2004a) investigated two-phase flow patterns of CO_2 in a 0.98 mm (0.0386 in.) single horizontal quartz glass tube. Heating was provided by applying a transparent, resistive, film coating on the glass, which allowed diabatic flow patterns to be observed. The dominant flow patterns observed were intermittent flow at low vapor qualities and wavy annular flow with entrainment of droplets at higher vapor qualities. Stratified flow was only observed at adiabatic test conditions. According to his observations, the mechanism of dryout was not related to the stratification of the flow but instead to liquid entrainment into the vapor core during annular flow.

Yun and Kim (2004) proposed a CO_2 two-phase flow pattern map based on their flow boiling visualizations of CO_2 in their horizontal, narrow rectangular channel. Transitions from bubbly-to-slug flow and from bubbly-to-annular flow were obtained by setting transition void fraction values of 0.2 and 0.35, respectively, using the drift-flux model of Wallis (1979) with flow distribution parameters of 1.11 and 1.05 for these two transitions, respectively (refer to the chapter on void fraction for information on the drift flux model). Assuming that the surface tension and inertial forces control the transition from slug-to-annular flow, they proposed a vapor Weber number criterion for this transition, the latter defined as a function of the superficial velocity of vapor phase U_G:

$$We_G = \frac{\rho_G U_G^2 d_i}{\sigma}$$
[19.2.1]

The slug-to-annular flow transition was set to occur when $We_G > 20$ where U_G is obtained from its definition:

$$U_G = \frac{\dot{Q}_G}{A}$$
[19.2.2]

Figure 19.1 shows that their map is largely successful in predicting the independent observations of Pettersen (2004a) for the slug-to-annular flow transition but not the two bubble flow observations. No droplet or mist flow criterion was proposed in their map so the three such observations in the graph cannot be checked.

Taking a different approach, the first flow pattern map for CO_2 of Cheng et al. (2006) was developed by modifying several of the flow pattern transition criteria of the Wotjan, Ursenbacher and Thome (2005a) flow pattern map for conventional refrigerants in order to improve its performance. Based in part on flow pattern data and in part on heat transfer data depicting sharp changes in the heat transfer coefficient that were attributed to flow transitions, the intermittent flow to annular flow (I-A) and the annular flow to dryout region (A-D) transition criteria were modified to better fit the CO_2 data. Other transition criteria remained the same as those of Wotjan, Ursenbacher and Thome (2005a) [refer to the chapter on flow pattern maps in this book to find a description of their map]. These modifications and some of their logic in making them are described below.
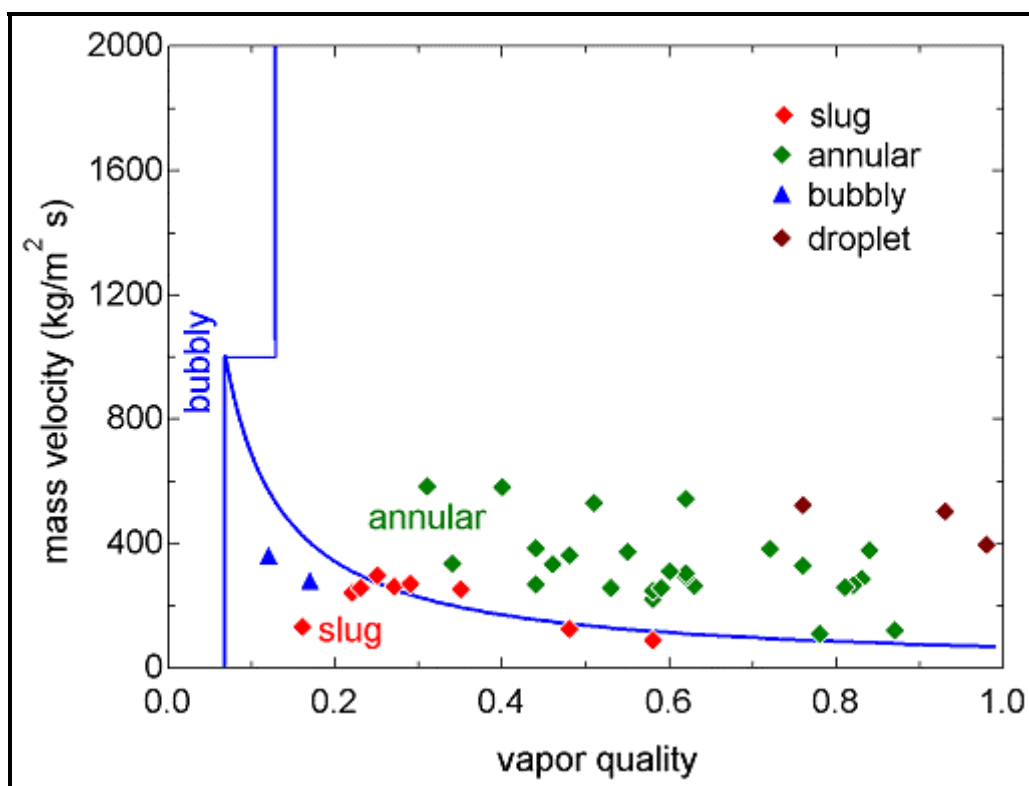
Figure 19.1. CO$_2$ flow pattern map proposed of Yun and Kim (2004) compared to the diabatic observations by Pettersen (2004a) (symbols) for tests at T$_{sat}$ = 20°C (68°F) and a tube diameter of 0.98 mm (0.0386 in.).

First of all, diabatic flow patterns are intrinsically related to the corresponding flow boiling heat transfer characteristics. Thus, the flow patterns can be used in part to physically explain the heat transfer mechanisms and characteristics. Vice versa, appropriate flow boiling heat transfer data can be used to back out the corresponding flow pattern transitions using one's intuition. For example, CO$_2$ has very large nucleate boiling heat transfer coefficients, much larger than the convective contribution to flow boiling at low vapor qualities. However, at somewhat higher vapor qualities (but still low qualities) the local flow boiling heat transfer coefficient of CO$_2$ actually tends to falloff noticeably (contrary to conventional refrigerants). This falloff can be intuitively ascribed to a change in the flow pattern from intermittent flow with its relatively thick liquid layers/liquid slugs in contact with the wall to annular flow with thin liquid films, the latter better adept to suppress nucleate boiling. Hence, the heat transfer results at low vapor quality can be used to try to interpret where the transition from intermittent-to-annular flow occurs. Another example is the onset of dryout, which is denoted by another very sharp drop in local flow boiling heat transfer coefficients and hence appropriate data can be used to distinguish between annular flow and the dryout region. Furthermore, the end of the dryout region and the beginning of mist flow is denoted by another sharp change in trend of the local heat transfer data. These trends are for instance very nicely illustrated by some flow boiling test results of Mori et al. (2000) for R-134a shown in Figure 19.2.
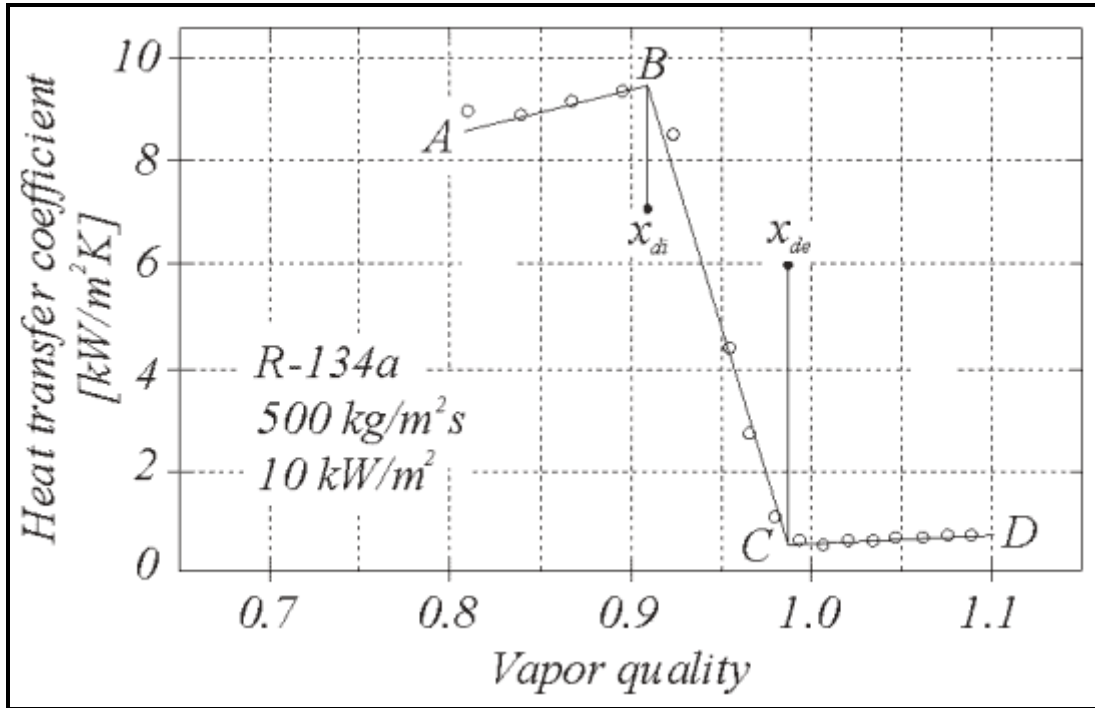
Figure 19.2. Flow boiling data of Mori et al. (2000) illustrating the sharp changes in trends in flow boiling data with vapor quality from annular flow to the dryout region and then to the mist flow regime

Analyzing CO_2 flow pattern observations and heat transfer data, new I-A and A-D transition criteria for the Wotjan, Ursenbacher and Thome (2005a) map were proposed by Cheng et al. (2006) for CO_2. The CO_2 I-A transition boundary is calculated as follows:

$$x_{IA} = \left[1.8^{1/0.875} \left(\rho_G / \rho_L \right)^{-1/1.75} \left(\mu_L / \mu_G \right)^{-1/7} + 1 \right]^{-1}$$ [19.2.3]

This boundary is extended downwards until it reaches the stratified flow transition boundary. The CO_2 A-D transition boundary is calculated as follows:

$$\dot{m}_{dryout} = \left\{ \frac{1}{0.67} \left[\ln \left(\frac{0.58}{x} \right) + 0.52 \right] \left(\frac{d_i}{\rho_G \sigma} \right)^{-0.17} \left[\frac{1}{g d_i \rho_G (\rho_L - \rho_G)} \right]^{-0.348} \left(\frac{\rho_G}{\rho_L} \right)^{-0.25} \left(\frac{q}{q_{DNB}} \right)^{-0.7} \right\}^{0.965}$$ [19.2.4]

In this equation, q_{DNB} is still calculated according to the Kutateladze (1948) correlation as before. The equation can also be solved for the vapor quality to find the value of x_{di} when inputting the mass velocity and other parameters.

The *second*, updated flow pattern map for CO_2 of Cheng et al. (2008a, 2008b) has been proposed by modifying the map above. As one of its expected applications is to automotive air-conditioning systems, it is important that it be valid up to very high mass velocities, in particular up to about 1500 kg/m²s (1,103,700 lb/h ft²) in channels with a diameter on the order of 1 mm (0.04 in.). Therefore, a CO_2 flow pattern map covering a much wider range of parametric conditions is needed to accurately predict the flow patterns for CO_2 evaporation in horizontal tubes. The changes to the above map are described below.

First of all, the annular flow to dryout (A-D) transition boundary is calculated with the following newly updated criterion based of the new dryout data for CO_2 added to their database:

$$\dot{m}_{dryout} = \left\{ \frac{1}{0.236} \left[\ln\left(\frac{0.58}{x}\right) + 0.52 \right] \left(\frac{d_i}{\rho_G \sigma}\right)^{-0.17} \left[\frac{1}{g d_i \rho_G (\rho_L - \rho_G)} \right]^{-0.17} \left(\frac{\rho_G}{\rho_L}\right)^{-0.25} \left(\frac{q}{q_{DNB}}\right)^{-0.27} \right\}^{1.471}$$

[19.2.5]

Extracting the vapor quality from the above expression, their new A-D dryout inception equation for x_{di} is

$$x_{di} = 0.58 \exp\left[0.52 - 0.236 We_G^{0.17} Fr_G^{0.17} \left(\frac{\rho_G}{\rho_L}\right)^{0.25} \left(\frac{q}{q_{DNB}}\right)^{0.27} \right]$$

[19.2.6]

The above equation remains the same as in the Wojtan, Ursenbacher and Thome flow map for low pressure refrigerants, except that new empirical parameters were obtained based on the CO_2 data. The departure from nucleate boiling heat flux q_{DNB} is calculated with the Kutateladze (1948) correlation. The vapor Weber number We_G and the vapor Froude number Fr_G defined by Mori et al. (2000) are used in the above expressions and are calculated as follows:

$$We_G = \frac{\dot{m}^2 d_i}{\rho_G \sigma}$$

[19.2.7]

$$Fr_G = \frac{\dot{m}^2}{\rho_G (\rho_L - \rho_G) g d_i}$$

[19.2.8]

Note that the definition of We_G here is based on the total flow rate of liquid plus vapor while [19.2.1] is based only on the vapor flow rate. The dryout region to mist flow (D-M) transition is calculated with the new criterion based on the new dryout completion data added to their database for CO_2:

$$\dot{m}_{mist} = \left\{ \frac{1}{0.502} \left[\ln\left(\frac{0.61}{x}\right) + 0.57 \right] \left(\frac{d_i}{\rho_G \sigma}\right)^{-0.16} \left[\frac{1}{g d_i \rho_G (\rho_L - \rho_G)} \right]^{-0.15} \left(\frac{\rho_G}{\rho_L}\right)^{0.09} \left(\frac{q}{q_{DNB}}\right)^{-0.72} \right\}^{1.613}$$

[19.2.9]

Extracting the vapor quality from this expression, their new dryout completion equation for x_{de} is

$$x_{de} = 0.61 \exp\left[0.57 - 0.502 We_G^{0.16} Fr_G^{0.15} \left(\frac{\rho_G}{\rho_L}\right)^{-0.09} \left(\frac{q}{q_{DNB}}\right)^{0.72} \right]$$

[19.2.10]

Note, however, that whenever the value of x_{di} or x_{de} is calculated to be larger than 1.0 using the extracted expressions above, the value is reset to 0.999. The vapor Weber number We_G and the vapor Froude number Fr_G are calculated as above. The bubbly-to-intermittent flow (I-B) transition is calculated with the same criterion as in the Kattan, Thome and Favrat (1998a) map, described in the chapter on flow pattern maps elsewhere in this book. This transition threshold is

$$\dot{m}_{bubbly} = \left\{ \frac{256\, A_{Gd}\, A_{Ld}^2\, d_i^{1.25}\, \rho_L (\rho_L - \rho_G) g}{0.3164 (1-x)^{1.75} \pi^2\, P_{id}\, \mu_L^{0.25}} \right\}^{1/1.75}$$

[19.2.11]

The dimensionless length of the stratified liquid interface P_{id} is calculated as a function of the stratified angle θ_{strat} (stratified angle around upper perimeter of the tube to stratified liquid level) as described in the chapter on flow pattern maps elsewhere in this book:

$$P_{id} = \sin\left(\frac{2\pi - \theta_{strat}}{2} \right)$$

[19.2.12]

The method for calculating θ_{strat} is given in the chapter on flow pattern maps. The logic for determining this transition is as follows: if $\dot{m} > \dot{m}_{bubbly}$ and $x < x_{IA}$, then the flow is bubbly flow (B). The following logic is applied to determine the other transitions in the high vapor quality range:

- If $\dot{m}_{strat}(x) \geq \dot{m}_{dryout}(x)$, then $\dot{m}_{dryout}(x) = \dot{m}_{strat}(x)$;
- If $\dot{m}_{wavy}(x) \geq \dot{m}_{dryout}(x)$, then $\dot{m}_{dryout}(x) = \dot{m}_{wavy}(x)$;
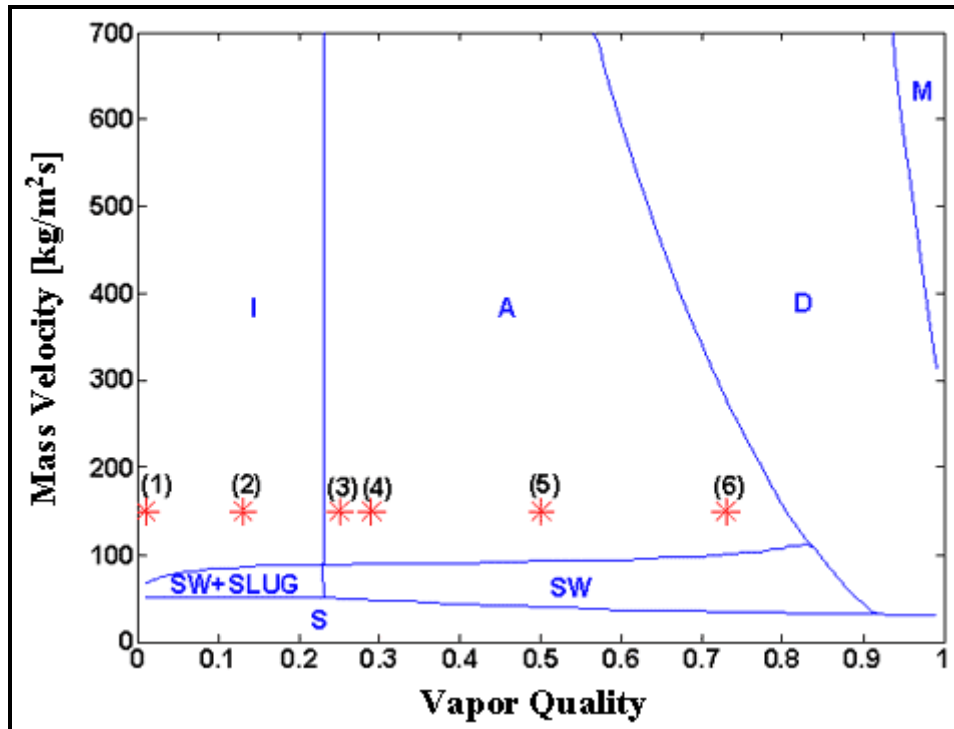- If $\dot{m}_{dryout}(x) \geq \dot{m}_{mist}(x)$, then $\dot{m}_{dryout}(x) = \dot{m}_{mist}(x)$.

Figure 19.3. The updated CO_2 flow pattern map of Cheng et al. (2008a) compared to the flow pattern observations of Gasche (2006) at a mass velocity of 149 kg/m²s (80,000 lb/h ft²), saturation temperature of 23.3°C (74°F), equivalent diameter of 0.833 mm (0.0328 in.) and heat flux of 1.86 kW/m² (590 Btu/h ft²) where he identified his observations as follows: plug flow (1, 2, 3, 4), slug/annular flow (5) and annular flow (6).

Figure 19.3 shows some of the recent CO_2 flow pattern results of Gashe (2006) observed during evaporation inside a 0.8 mm (0.0315 in.) equivalent diameter rectangular channel compared to the updated CO_2 flow pattern map. It should be mentioned that the slug/annular flow designation of Gashe is shown as an annular flow here since from his photographs it seems that the annular flow is the predominant pattern. [Note: you can see some in Cheng et al. (2008a).] His observations (3) and (4) are near their correct regimes. All together, about 80% of his total of 28 observations was identified correctly by the updated flow map (his plug flow is apparently equivalent to our intermittent flow regime). Note that the bubbly flow regime is not observed here as it lies at higher mass velocities than shown in the map.

19.3 Two-Phase Pressure Drops and Prediction Methods for CO_2

Thome and Ribatski (2005) and Cheng et al. (2008a) made a comprehensive literature study on experimental two-phase pressure drops of CO_2 and their work is summarized here. Five independent experimental studies [1 study on a macroscale channel when $d_i > 3$ mm (0.118 in.) and 4 studies on microscale channels when $d_i \leq 3$ mm, as categorized here] from different laboratories were used to form their database. The database included experimental data from Bredesen et al. (1997), Pettersen (2004b), Zhao et al. (2000) and Yun and Kim (2003a). The details of the test conditions are summarized in Table 19.1. The test channels included single circular channels and multi-channels with circular, triangular and rectangular cross-sections. It must be pointed out that some authors created confusion because they did not cite if their data were for two-phase *frictional* pressure drops or *total* two-phase pressure drops (that include the momentum pressure drop in evaporation in a horizontal tube) and thus their data could not be utilized while other data were presented in a form precluding their extraction from their publication (such as presenting the data only in correlated format). Regrettably, about 80% of the data points come from only one paper in the database, that of Bredesen et al. (1997), and hence the database should be enlarged with other independent data when possible in the future.

Table 19.1. CO2 pressure drop database

Study	Channel Configuration Material	Diameter (mm)*	T_{sat} (°C)	Reduced Pressure	Mass Velocity (kg/m²s)	Heat Flux (kW/m²)	Data Points	Heating Method
Bredesen et al. (1997)	Single circular tube, stainless steel	7	-25 -10 5	0.21 0.37 0.54	200, 300, 400	3, 6, 9	319	Electrical heating
Pettersen (2004b)	Multi-channel with 25 circular channels, aluminum	0.8	0 10 20	0.47 0.61 0.78	190, 280, 380	10	24	Heated by water
Zhao et al. (2000)	Multi triangular channels, stainless steel	1.15 (0.86)*	10	0.61	300	11	9	Electrical heating
Yun and Kim (2003a)	Multi-rectangular channels	1.74 (1.53)*	5	0.54	200, 300, 400	15	15	Electrical heating

∗ The value in the parentheses is the hydraulic diameter for non-circular channels while the first value is the equivalent diameter.

The two-phase frictional pressure drop methods by Chisholm (1973), Friedel (1979), Grönnerud (1972), Müller-Steinhagen and Heck (1986), a modified Chisholm correlation by Yoon et al. (2004) and the flow pattern based model by Moreno Quibén and Thome (2007a, 2007b) were compared to this database. Three criteria were used to analyze the accuracy of the methods: the standard deviation, the mean error and the percent of data predicted within ±30%. The statistical results are summarized in Table 19.2. None

of these methods is able to predict the CO_2 two-phase frictional pressure drop data all that well (however, note that all have been extrapolated beyond their original conditions to make this comparison for CO_2). The Friedel method overall gave reasonable predictions but worked poorly for the smaller channel data.

Table 19.2. Results for the two-phase frictional pressure drop predictions.

Method	Percentage of Predicted Points within ±30 %	Mean Error	Standard Deviation
Chisholm (1973)	56.1 %	48.6 %	73.8 %
Friedel (1979)	71.1 %	30.9 %	55.8 %
Grönnerud (1972)	30.2 %	75 %	113.1 %
Müller-Steinhagen and Heck (1986)	55.8 %	33.3 %	44.3 %
Modified Chisholm by Yoon et al. (2004)	47 %	34.7%	93.7%
Moreno Quibén and Thome (2007a, 2007b)	42.4 %	50.1%%	90.6%
Cheng et al. (2008a)	74.7 %	28.6%	44.3%

To try to improve on this situation, and to better reflected the effects of channel diameter and flow regimes, a new updated two-phase frictional pressure drop model for CO_2 was proposed by Cheng et al. (2008a) by modifying the flow pattern based model of Moreno Quibén and Thome (2007a, 2007b), which was originally developed from a R-22, R-410a and R-134a database for macroscale channels. In doing this, they incorporated the updated CO_2 flow pattern map of Cheng et al. (2008a) described above into this model. The original Moreno Quibén-Thome model is described in the pressure drop chapter in this book.

The updated two-phase flow frictional pressure drop model of Cheng et al. (2008a) for CO_2 is implemented using the equivalent diameter for d_i for non-circular tubes to remain consistent with the associated flow pattern map. The advantage of using the equivalent diameter is that it gives the same mass velocity as in the original non-circular channel whilst the hydraulic diameter does not, and thus it correctly reflects the mean liquid and vapor velocities using the void fraction in the calculations. Their prediction methods are described below, flow pattern by flow pattern.

CO_2 frictional pressure drop model for annular flow (A): The basic equation is the same as that of the Moreno-Quibén-Thome pressure drop model:

$$\left(\frac{dp}{dz}\right)_{annular} = 2(f_i)_{annular} \frac{\rho_G u_G^2}{d_i} \qquad [19.3.1]$$

The two-phase flow friction factor for annular flow $(f_i)_{annular}$ was correlated using the CO_2 experimental data identified to fall within the annular flow regime by the flow pattern map:

$$(f_i)_{annular} = 3.128 \, Re_G^{-0.454} \, We_L^{-0.0308} \qquad [19.3.2]$$

This friction factor correlation is quite different from that of the Moreno Quibén-Thome model. The mean velocity of the vapor phase u_G is calculated as

$$u_G = \frac{\dot{m}x}{\rho_G \varepsilon} \qquad\qquad [19.3.3]$$

The void fraction ε is calculated using the Steiner (1993) version of the drift flux model of Rouhani and Axelsson (1970):

$$\varepsilon = \frac{x}{\rho_G}\left[\left(1+0.12(1-x)\right)\left(\frac{x}{\rho_G}+\frac{1-x}{\rho_L}\right)+\frac{1.18(1-x)[g\sigma(\rho_L-\rho_G)]^{0.25}}{\dot{m}\rho_L^{0.5}}\right]^{-1} \qquad [19.3.4]$$

The vapor phase Reynolds number Re_G, the liquid phase Weber number We_L and the mean liquid velocity u_L are calculated as

$$Re_G = \frac{\dot{m}xd_i}{\mu_G \varepsilon} \qquad\qquad [19.3.5]$$

$$We_L = \frac{\rho_L u_L^2 d_i}{\sigma} \qquad\qquad [19.3.6]$$

$$u_L = \frac{\dot{m}(1-x)}{\rho_L(1-\varepsilon)} \qquad\qquad [19.3.7]$$

CO₂ frictional pressure drop model for slug and intermittent flows (Slug+I): One method is used for both flow regimes. A linear interpolation between the all liquid limit and annular flow is used to avoid any jump in the predicted values at the transition between these two flow patterns and the annular flow regime. The Moreno Quibén-Thome model was updated by removing its exponents to become:

$$\left(\frac{dp}{dz}\right)_{slug+intermittent} = \left(\frac{dp}{dz}\right)_L\left(1-\frac{\varepsilon}{\varepsilon_{IA}}\right)+\left(\frac{dp}{dz}\right)_{annular}\left(\frac{\varepsilon}{\varepsilon_{IA}}\right) \qquad [19.3.8]$$

The annular flow pressure gradient is calculated as above. The single phase frictional pressure drop, considering the total vapor-liquid flow as liquid flow, is calculated as

$$\left(\frac{dp}{dz}\right)_L = 2f_L\frac{\dot{m}^2}{\rho_L d_i} \qquad\qquad [19.3.9]$$

The liquid friction factor f_L and the liquid Reynolds number to use in this expression are obtained from

$$f_L = \frac{0.079}{Re_L^{0.25}} \qquad\qquad [19.3.10]$$

$$Re_L = \frac{\dot{m}d_i}{\mu_L} \qquad\qquad [19.3.11]$$

The all liquid flow pressure gradient $(dp/dz)_L$ is calculated assuming all the flow liquid and using liquid properties while $(dp/dz)_{annular}$ is the annular flow frictional pressure gradient using the actual vapor quality x of the slug or intermittent flow (not x_{IA}) in its evaluation with $\theta_{dry} = 0$ and also the actual value of x is used to calculate ε. At the limit of x = 0, this expression correctly reduces to that of an all-liquid turbulent flow (or laminar flow but no such data were in their database) while at x = x_{IA} it goes to the annular flow prediction without a jump in value at the transition. The value of ε_{IA} is obtained by evaluating its expression with x set equal to x_{IA}.

CO₂ frictional pressure drop model for stratified-wavy flow (SW): The equation is kept the same as in the original model, that is:

$$\left(\frac{dp}{dz}\right)_{stratified-wavy} = 2\left(f_i\right)_{stratified-wavy}\frac{\rho_G u_G^2}{d_i} \qquad [19.3.12]$$

However, the two-phase friction factor for stratified-wavy flow $(f_i)_{stratified-wavy}$ is calculated with the following modified interpolating expression based on the CO₂ database:

$$\left(f_i\right)_{stratified-wavy} = \theta_{dry}^{*~0.02} f_G + \left(1 - \theta_{dry}^*\right)^{0.02}\left(f_i\right)_{annular} \qquad [19.3.13]$$

The dimensionless dry angle θ_{dry}^* is defined as

$$\theta_{dry}^* = \frac{\theta_{dry}}{2\pi} \qquad [19.3.14]$$

θ_{dry} is the dry angle and is defined the same as in the original model. The dry angle θ_{dry} is used to determine the fraction of the tube perimeter in contact with only vapor, which has a significantly different pressure gradient than the wetted perimeter. For the stratified-wavy regime (SW), the original equation is used for its calculation together with the transition equations of the flow pattern map calculated at the same vapor quality, such that:

$$\theta_{dry} = \left[\frac{\dot{m}_{wavy} - \dot{m}}{\dot{m}_{wavy} - \dot{m}_{strat}}\right]^{0.61}\theta_{strat} \qquad [19.3.15]$$

The stratified angle θ_{strat} is calculated using the void fraction obtained from [19.3.4] in the expression for θ_{strat} in Chapter 13. The vapor-phase friction factor f_G is obtained using the definition of Re_G above and using

$$f_G = \frac{0.079}{Re_G^{0.25}} \qquad [19.3.16]$$

CO₂ frictional pressure drop model for slug-stratified wavy flow (Slug+SW): The updated expression here without the exponents is:

$$\left(\frac{dp}{dz}\right)_{slug+SW} = \left(\frac{dp}{dz}\right)_L\left(1 - \frac{\varepsilon}{\varepsilon_{IA}}\right) + \left(\frac{dp}{dz}\right)_{stratified-wavy}\left(\frac{\varepsilon}{\varepsilon_{IA}}\right) \qquad [19.3.17]$$

The two pressure gradients are calculated using the requisite expressions above. The all liquid flow pressure gradient $(dp/dz)_L$ is calculated assuming all the flow is liquid and using liquid properties while $(dp/dz)_{stratified-wavy}$ is calculated using the actual vapor quality x (not x_{IA}) and also the actual value of x is used to calculate ε. At the limit of x = 0, this expression correctly reduces to that of an all-liquid turbulent flow (or laminar flow but no such data were in their database) while at x = x_{IA} it goes to the stratified-wavy flow prediction without a jump in value at the transition. The value of ε_{IA} is obtained by evaluating its expression with x set equal to x_{IA}. Refer to the original model for other details in the chapter on two-phase pressure drops.

CO₂ frictional pressure drop model for mist flow (M): The following expression is kept the same as in the original model, i.e. the homogeneous model:

$$\left(\frac{dp}{dz}\right)_{mist} = \frac{2(f_i)_{mist}\,\dot{m}^2}{d_i\rho_H} \qquad [19.3.18]$$

The homogenous density ρ_H is

$$\rho_H = \varepsilon_H\rho_G + (1-\varepsilon_H)\rho_L \qquad [19.3.19]$$

The homogenous void fraction ε_H is calculated as

$$\varepsilon_H = \frac{1}{1+\left(\dfrac{(1-x)}{x}\dfrac{\rho_G}{\rho_L}\right)} \qquad [19.3.20]$$

The new friction factor correlation for mist flow was developed specifically according to the CO₂ experimental data. The friction factor may be expressed in terms of the homogeneous Reynolds number as:

$$(f_i)_{mist} = \frac{91.2}{Re_H^{0.832}} \qquad [19.3.21]$$

where the homogeneous Reynolds number is

$$Re_H = \frac{\dot{m}d_i}{\mu_H} \qquad [19.3.22]$$

The homogeneous viscosity expression used for calculating this homogeneous Reynolds number is:

$$\mu_H = x\mu_G + (1-x)\mu_L \qquad [19.3.23]$$

The constants in mist flow friction factor expression were obtained from the fit to the mist flow pressure drop data, which are quite different from those in the Blasius equation. The reason is possibly because of the effect of the droplets impinging on the channel wall and their effect on the velocity gradient near the

wall. More experimental data should be obtained for the mist flow regime to further verify this correlation or modify it in the future if necessary.

CO₂ frictional pressure drop model for dryout region (D): The linear interpolating expression is kept the same as that in the original Moreno Quibén-Thome model:

$$\left(\frac{dp}{dz}\right)_{dryout} = \left(\frac{dp}{dz}\right)_{x=x_{di}} - \frac{x - x_{di}}{x_{de} - x_{di}}\left[\left(\frac{dp}{dz}\right)_{x=x_{di}} - \left(\frac{dp}{dz}\right)_{x=x_{de}}\right]$$

[19.3.24]

Here, $(dp/dz)_{x=x_{di}}$ is the frictional pressure drop at the dryout inception quality x_{di} calculated with the expression for annular flow or stratified-wavy flow whereas $(dp/dz)_{x=x_{de}}$ is the frictional pressure drop at the completion quality x_{de} and is calculated with the mist flow expression. The values of x_{di} and x_{de} are calculated with the updated expressions of Cheng et al. (2008a) given earlier in this chapter.

CO₂ frictional pressure drop model for stratified flow (S): None of the database fell into this regime, but for the sake of completeness, the method of the Moreno Quibén-Thome model is applied as follows:

If $x_{IA} \leq x \leq x_{di}$, then the friction factor for stratified flow is calculated as:

$$(f_i)_{stratified} = \theta^*_{strat} f_G + \left(1 - \theta^*_{strat}\right)(f_i)_{annular}$$

[19.3.25]

Similar to the method for stratified-wavy flow, the single-phase vapor friction factor is calculated in the same manner as noted above and the friction factor for the lower wetted fraction of the perimeter of the tube $(f_i)_{annular}$ is calculated using the annular flow expression with the actual vapor quality in the calculation. Meanwhile, the value of θ_{dry} becomes θ_{strat}, such that:

$$\theta^*_{strat} = \frac{\theta_{strat}}{2\pi}$$

[19.3.26]

The frictional pressure gradient for stratified flow then is obtainable from:

$$\left(\frac{dp}{dz}\right)_{stratified(x \geq x_{IA})} = 2(f_i)_{stratified}\frac{\rho_G u_G^2}{d_i}$$

[19.3.27]

If $0 \leq x < x_{IA}$, then the frictional pressure gradient for stratified flow is given by the following linear interpolation rather than the exponential expression of the Moreno Quibén-Thome model so as to avoid a jump at the upper boundary of this zone:

$$\left(\frac{dp}{dz}\right)_{stratified(x<x_{IA})} = \left(\frac{dp}{dz}\right)_L\left(1 - \frac{\varepsilon}{\varepsilon_{IA}}\right) + \left(\frac{dp}{dz}\right)_{stratified(x \geq x_{IA})}\left(\frac{\varepsilon}{\varepsilon_{IA}}\right)$$

[19.3.28]

For details on its implementation, refer to the Moreno Quibén-Thome model in the chapter on two-phase pressure drops elsewhere in this book.

CO₂ frictional pressure drop model for bubbly flow (B): To remain consistent with the frictional pressure drops in the neighboring regimes without creating a jump at the transition (no bubbly flow model was proposed in the Moreno-Quibén-Thome pressure drop model), the following expression is used:

$$\left(\frac{dp}{dz}\right)_{bubbly} = \left(\frac{dp}{dz}\right)_{L}\left(1-\frac{\varepsilon}{\varepsilon_{IA}}\right)+\left(\frac{dp}{dz}\right)_{annular}\left(\frac{\varepsilon}{\varepsilon_{IA}}\right) \qquad [19.3.29]$$

Experimental data should be obtained to verify or modify this regime's method.
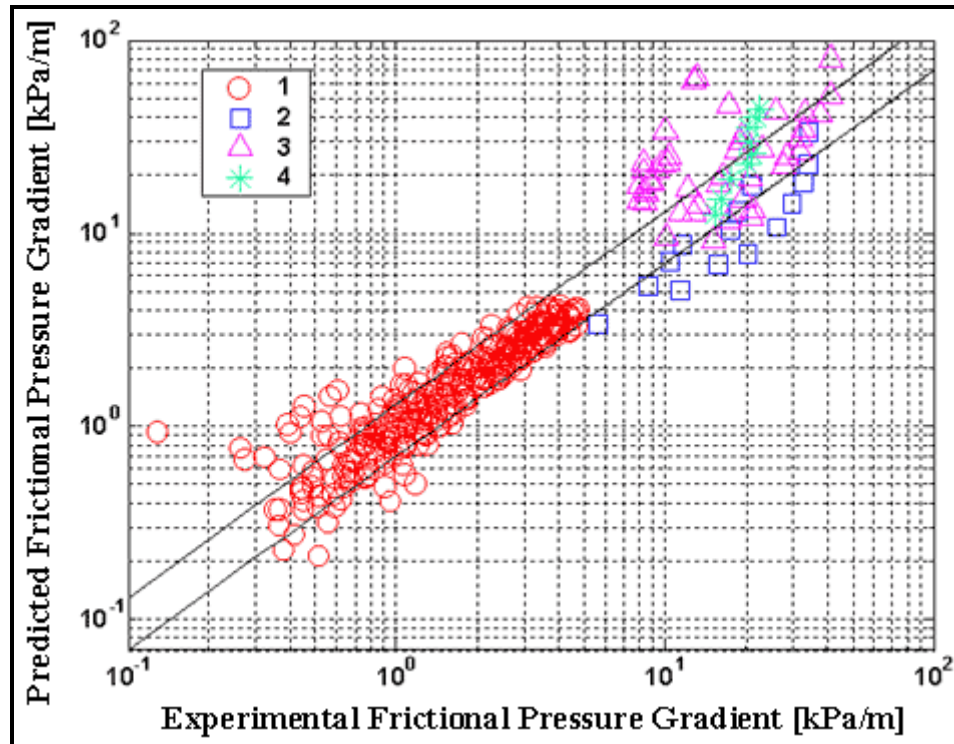
Figure 19.4. Frictional pressure gradients predicted by the Cheng et al. (2008a) model compared to the entire database by individual study. The following percent of data are captured with ±30%: 1-Bredesen et al. (1997) 82%; 2-Yun and Kim (2003a) 33%; 3-Pettersen (2004b) 43%; 4-Zhao et al. (2000) 56%. Note that 2, 3 and 4 are the data for smaller channels.

Figure 19.4 shows the comparison of the new pressure drop model to the entire experimental database described in Table 19.1. As shown in Table 19.2, the new CO_2 two-phase frictional pressure drop model predicts the CO_2 pressure drop data better than other existing empirical methods, but only marginally better than the Friedel method. Specifically, the new model predicts 81.5% of the macroscale data to within ±30% whereas the Friedel method predicts 77%. For the microscale data, the new model predicts only 44% of the microscale data to within ±30% and the Friedel method predicts only 35%. Thus, neither method is currently proven to be sufficient for the prediction of microchannel pressure drop data, possibly because there are very limited experimental data points. Experimentally, it is more difficult to measure such data without disturbing the flow itself, for instance the microchannel experimental data sets in the present data base have a scatter of up to 50% which makes it difficult to achieve good statistics in their prediction. As can be seen in Figure 19.4, the Cheng et al. model goes through the center of the scatter in

these data. Thus, more accurate experimental data for a wider range of tests conditions are required to advance this prediction method, especially data at high vapor qualities and for microchannels.

19.4 Flow Boiling Heat Transfer and Prediction Methods for CO_2

In Cheng et al. (2006), it was found that the CO_2 prediction methods by Wang et al. (2003) and Yoon et al. (2003, 2004) were not satisfactory when compared to independently measured macrochannel experimental flow boiling data. These correlations were developed essentially with the authors' own database and do not extrapolate well when applied to other channel sizes and test conditions confronted in the other experimental studies. Furthermore, the CO_2 specific method proposed by Thome and El Hajal (2004) was found to only worked reasonably well at low vapor qualities when compared to the new independent flow boiling data. Cheng et al. also found that both microscale and macroscale prediction methods performed poorly when compared against independent small diameter tube data. For instance, the three-zone microchannel flow boiling model presented in the two-part paper of Thome, Jacobi and Dupont (2004) and Dupont, Thome and Jacobi (2004) included one study of CO_2 in its database; however, it did not work all that well when compared to new CO_2 microchannel flow boiling results, perhaps because the 3-zone model only treats elongated bubble flow while most of the new data are in annular flow and include some post dryout heat transfer data.

Based on this situation, Cheng et al. (2006) proposed an updated flow pattern map and flow boiling model for CO_2 whose broader flow boiling database covered experimental results from six independent studies obtained for mass velocities from 80 to 570 kg/m²s (5886 to 419410 lb/h ft²), heat fluxes from 5 to 32.1 kW/m² (1585 to 10170 Btu/h ft²), saturation temperatures from –28 to 25°C (-18.4 to 77°F) [the corresponding reduced pressures are from 0.21 to 0.87] and tube diameters from 0.8 to 10.06 mm (0.0315 to 0.396 in.). All the experiments were conducted in horizontal tubes. Their new heat transfer model was developed specially for CO_2 in tandem with their new CO_2 map described earlier. As the starting point, the model developed by Wojtan, Ursenbacher and Thome (2005a, 2005b) was used, which is an updated version of the flow pattern maps and flow boiling heat transfer models of Kattan, Thome and Favrat (1998a, 1998b, 1998c) and Thome and El Hajal (2004). The new proposed prediction method includes a new correlation for nucleate boiling heat transfer and a boiling suppression factor was added. In addition, a new dryout inception vapor quality correlation for x_{di} was proposed for CO_2 and accordingly the heat transfer predictions in the dryout region were improved by better identification of one of this regime's boundaries. The changes to the Wojtan-Ursenbacher-Thome conventional refrigerant model are described below.

First of all, the general expression for the local flow boiling heat transfer coefficient in a horizontal tube remains the same as in the original model, that is:

$$\alpha_{tp} = \frac{\theta_{dry}\alpha_{vapor} + (2\pi - \theta_{dry})\alpha_{wet}}{2\pi} \qquad [19.4.1]$$

However, the wet wall expression for α_{wet} was modified to introduce a boiling suppression factor S into the model, similar to classic model of Chen (1963):

$$\alpha_{wet} = \left((S\alpha_{nb})^3 + \alpha_{cb}^3\right)^{1/3} \qquad [19.4.2]$$

Nucleate boiling heat transfer correlation for CO_2. The experimental flow boiling heat transfer data at vapor qualities $x < x_{IA}$ in the CO_2 database were used to extract the nucleate boiling contribution by

removing their convective heat transfer contributions using the above equations to develop a nucleate boiling database for CO_2. The Cooper (1984) correlation was found to greatly under predict these data at low heat fluxes while the correlation of Gorenflo (1993) tended to over predict the data. Thus, the following new nucleate boiling heat transfer correlation for CO_2 was proposed until a better method comes along:

$$\alpha_{nb} = 131 p_r^{-0.0063} \left(- \log_{10} p_r\right)^{-0.55} M^{-0.5} q^{0.58}$$ [19.4.3]

This expression is a dimensional correlation, giving α_{nb} in W/m^2K where p_r is the reduced pressure, M is the molecular weight of CO_2 and q is the heat flux at the tube wall input in W/m^2. This nucleate boiling heat transfer correlation for CO_2 predicted about 90% of the data within $\pm$ 20%. The database was formed from the CO_2 flow boiling data that fell into the intermittent and slug flow regimes according to their map, with the convective contribution subtracted out while setting S = 1 for no suppression in these two regimes. A comparison of this method to its database can be found in its original publication.

Nucleate boiling suppression factor correlation for CO_2. As nucleate boiling heat transfer is suppressed by the steeper temperature gradient in the liquid film in an annular flow as per the theory of Chen (1966), a boiling suppression factor correlation is needed in the flow boiling heat transfer model for CO_2 to capture this effect. Unlike other earlier boiling suppression factor correlations, which were empirically correlated based on the Lockhart-Martinelli number, Reynolds number, Boiling number and Prandt number, the liquid film thickness was used as a main parameter by Cheng et al. (2006) since it was found by analysis of their "suppression data" to have a significant effect on the values of S backed out of their flow boiling database. Incorporating also the effect of tube diameter, the following boiling suppression factor correlation was obtained for CO_2:

If $x < x_{IA}$, $S = 1$ [19.4.4a]

If $x \geq x_{IA}$, $S = 1 - 1.14 \left(d_i / d_{ref}\right)^2 \left(1 - \delta / \delta_{IA}\right)^{2.2}$ [19.4.4b]

The value of the reference diameter d_{ref} is equal to 0.00753 m except when $d_i > 0.00753$ m, then d_i/d_{ref} is set equal to 1.0 in this expression. For non-circular channels, the equivalent diameter is used. The film thicknesses δ and δ_{IA} are obtained from the geometrical expression using their respective values for the void fraction and dry angle at x and x_{IA}:

$$\delta = \frac{d_i}{2} - \left[\left(\frac{d_i}{2}\right)^2 - \frac{(1-\varepsilon)\pi d_i^2}{2(2\pi - \theta_{dry})}\right]^{1/2}$$ [19.4.5]

Dryout region heat transfer correlation for CO_2. When developing their boiling suppression factor correlation, dryout data were determined using the boiling suppression factors backed out from all the individual heat transfer data points using the general expression above. Negative boiling suppression factor values were taken as identifying dryout heat transfer data points and those giving boiling suppression factor values around zero were taken as indicating the onset of the dryout. Based on these dryout inception data, the new dryout inception vapor quality correlation for x_{di} was developed, giving the new annular to dryout region (A-D) transition boundary for CO_2, has been described earlier in this chapter. Other than this new expression affecting the vapor quality of the last local heat transfer coefficient at the end of the annular flow regime, the dryout region heat transfer prediction method remained the same.

Figure 19.5 illustrates a simulation of the new flow pattern map and heat transfer model of Cheng et al. (2006). In the left diagram, Arrow 1 shows the change of I-A transition boundary and arrow 2 shows the change of A-D transition boundary. Arrow 3 shows the corresponding movement of the S-SW/SW+Slug boundary when shifting the I-A boundary to the left. Note that at these conditions, the onset of dryout occurs already at a vapor quality of 0.68. In the right diagram, some experimental flow boiling data are plotted and compared to the new CO_2 heat transfer model and the Wojtan-Thome-Ursenbacher model, highlighting in part why a new method specific to CO_2 is required. As can be ascertained from the flow pattern map on the left, 3 of the heat transfer data points fall in the annular flow regime and 3 in the dryout regime, where they fall off sharply in value.
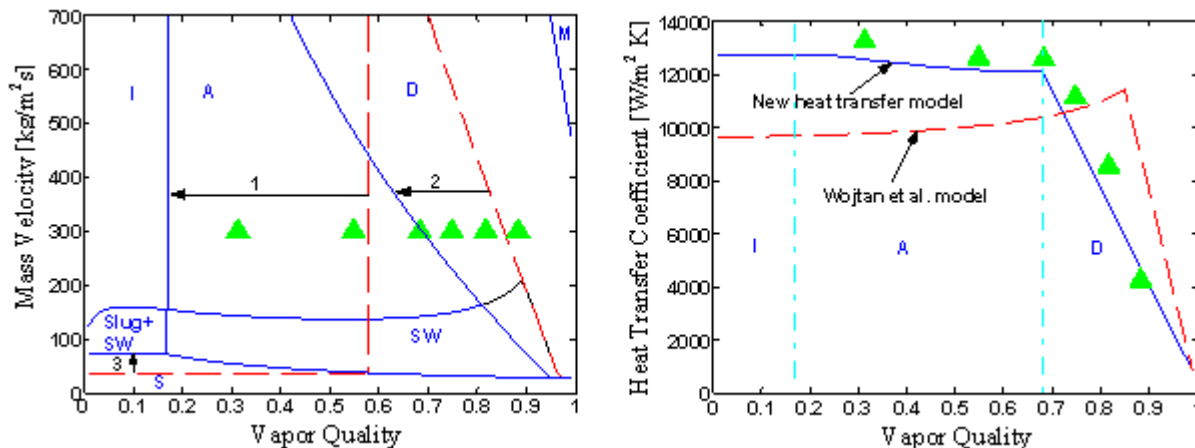
Figure 19.5. Flow pattern map of Cheng et al. (2006) for CO^2 applied to an internal diameter of 1.54 mm, mass velocity of 300 kg/m^{2}s, saturation temperature of 5 °C and heat flux of 20 kW/m2). *Left***: The new flow pattern transition boundaries (blue lines) for CO_2 and the flow pattern transition boundaries (red lines) of Wojtan-Ursenbacher-Thome compared at the test conditions of Yun, Kim and Kim (2005a) denoted by the triangles.** *Right***: The experimental flow boiling heat transfer coefficients of Yun, Kim and Kim (2005a) are compared to the Cheng et al. (2006) model (blue lines) and that of Wojtan-Ursenbacher-Thome (red lines), showing also the predicted flow pattern transition boundaries (turquoise lines).**

Figure 19.6 shows another example of the heat transfer model compared to one of the individual data sets in their database. The vertical lines in the graph delineate the flow pattern transition boundaries predicted by the map. Note that the heat transfer coefficient tends to be flat at low vapor qualities where nucleate boiling dominants but is not suppressed in the intermittent flow regime. Then, the boiling suppression kicks in when the flow becomes annular, reducing the heat transfer coefficients quite sharply in this case. At high vapor qualities in the annular flow regime, the convective boiling contribution grows to be noticeable in the curve, creating the minimum and upswing of the prediction. Then, the onset of dryout is reached at the peak, followed by a further decline in heat transfer in the dryout regime.

In summary, the Cheng et al. (2006) heat transfer model predicted 75.5% of its CO_2 database (318 data points) to within ± 30% and 79.1% of the CO_2 database (287) to within ± 30% without the dryout data points.
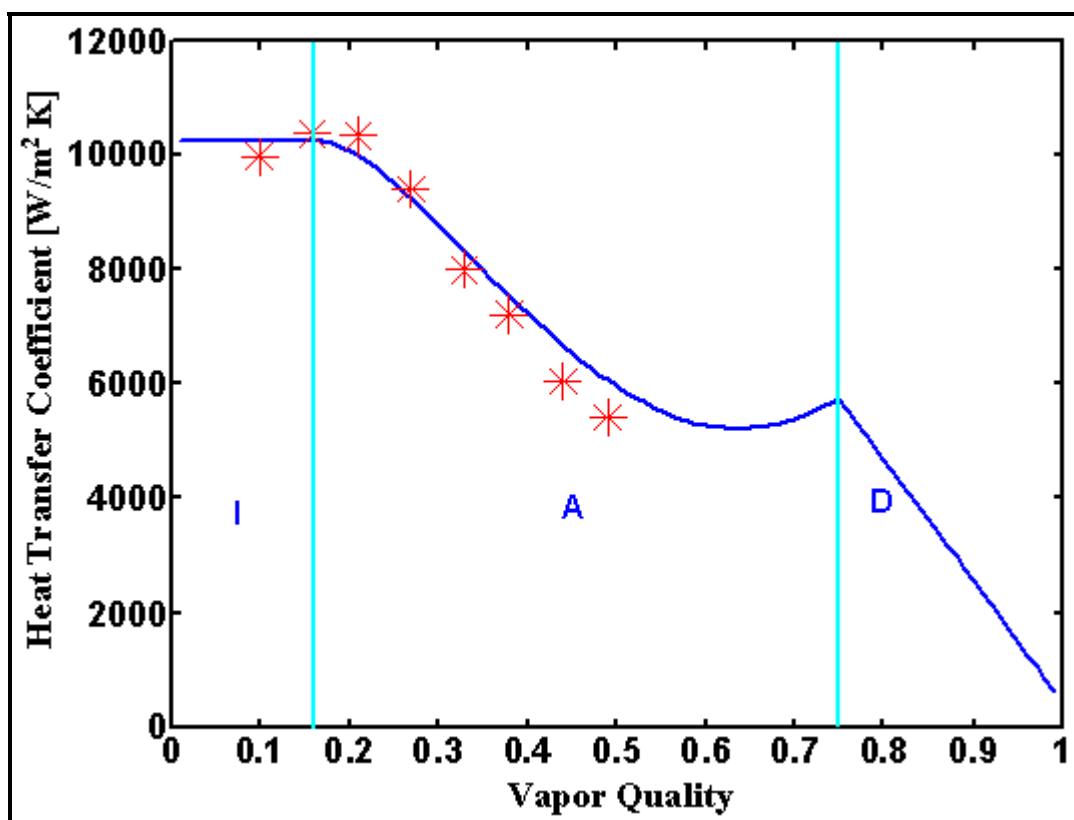
Figure 19.6. Flow boiling heat transfer coefficients predicted with the Cheng et al. (2006) model of Yoon et al. (2004) for a diameter of 7.53 mm, a saturation temperature of 0 °C, a mass velocity of 318 kg/m²s and heat flux of 16.4 kW/m². The vertical turquoise lines show the predicted flow pattern transition boundaries.

Numerous new CO_2 flow boiling data became available since the above study was completed, so a new updated flow pattern map and updated general flow pattern based flow boiling heat transfer model were developed by Cheng et al. (2008a, 2008b) using the Cheng et al. (2006) methods as the starting basis. In the Cheng et al. (2008b) heat transfer model, a new mist flow heat transfer correlation for CO_2 was developed based on the larger CO_2 database and a heat transfer method for bubbly flow was proposed for completeness sake since heat exchanger simulations sometimes hit this regime. The heat transfer predictions in the dryout regime are thus also updated since they use the mist flow correlation as the end point in their linear interpolation. All the flow regimes in the flow pattern map are thus covered in the new updated general flow boiling heat transfer model for CO_2. The database covered by the new heat transfer model handles a wider range of conditions for horizontal tubes and is described in Table 19.3. The range of parameters is as follows:

- tube diameters from 0.6 to 10.06 mm (0.024 to 0.396 in.);
- mass velocities from 50 to 1500 kg/m²s (36,790 to 1,103,700 lb/h ft²);
- heat fluxes from 1800 to 46,000 W/m² (571 to 14,585 Btu/h ft²);
- saturation temperatures from -28°C to +25°C (-18.4°F to +77.0°F);
- saturation pressures from 15.5 to 64.2 bars (225 to 931 psia);
- reduced pressures from 0.21 to 0.87.

Table 19.3. Heat transfer database for CO2 used by Cheng et al. (2008a, 2008b).

Data Source	Channel Configuration Material	Diameter (mm)[+]	T_{sat} (°C)	Reduced Pressure	Mass Flux (kg/m²s)	Heat Flux (kW/m²)	Data Points	Heating Method
*Knudsen and Jensen (1997)	Single circular tube, stainless steel	10.06	-28	0.21	80	8, 13	16	Heated by condensing R-22 vapor
*Yun et al. (2003)	Single circular tube, stainless steel	6	5, 10	0.54, 0.61	170, 240, 340	10, 15, 20	53	Electrical heating
*Yoon et al. (2004)	Single circular tube, stainless steel	7.53	0, 5, 10, 15, 20	0.47, 0.54, 0.61, 0.69 0.78	318	12.5, 16.4, 18.6	127	Electrical heating
*Koyama et al. (2001)	Single circular tube, stainless steel	1.8	0.26, 9.98, 10.88	0.47, 0.61, 0.62	250, 260	32.06	36	Electrical heating
*Pettersen (2004b)	Multi-channel of 25 circular channels, aluminium	0.8	0, 10, 20, 25	0.47, 0.61, 0.78, 0.87	190, 280, 380, 570	5, 10, 15, 20	46	Heated by water
*Yun, Kim and Kim (2005a)	Multi-channels with rectangular channels, material not mentioned	1.52 (1.14) 1.74 (1.53) 1.81 (1.54)	5	0.54	200, 300, 400	10, 15, 20	56	Electrical heating
Gao and Honda (2005a, 2005b)	Single circular tube, stainless steel	3	-7, 10	0.39, 0.61	236, 390, 393, 590, 786, 1179	10, 20, 21	150	Electrical heating
Tanaka et al. (2001)	Single circular tube, stainless steel	1	15	0.69	360	9, 18, 36	119	Electrical heating
Hihara (2000)	Single circular tube, stainless steel	1	15	0.69	720, 1440	9, 18, 36	150	Electrical heating
Shinmura, Take and Koyama (2006)	Multi-channel with circular channels, Aluminum	0.6	5.83	0.55	400	10, 20	48	Heated by water
Zhao et al. (2000)	Multi-channel with triangular channels, Aluminum	1.15 (0.86)	10	0.61	300	11	11	Electrical heating
Yun, Choi and Kim (2002) and Yun, Kim and Kim (2005b)	Single circular channel	0.98, 2	5, 10	0.54, 0.61	1000, 1500	7.2, 7.3, 15.9, 16.2, 20, 26, 26.5, 30, 36, 46	224	Electrical heating
Jeong, Cho and Kim (2005)	Multi-channel with rectangular channels, Aluminum	2.3 (2)	0, 5, 10	0.47, 0.54, 0.61	450, 600, 750	4, 8, 12	88	Electrical heating

[*] The data used in the previous study of Cheng et al. (2006). [+] Values in the parentheses are hydraulic diameters while the first value is equivalent diameter for non-circular channels.

Here, the new mist flow heat transfer correlation of Cheng et al. (2008b) is described. The heat transfer coefficient in mist flow of CO_2 is calculated by their new version of the Groeneveld (1973) correlation, using the CO_2 data identified in their database as being in this regime, which is as follows:

$$\alpha = 2 \times 10^{-8} \, Re_H^{1.97} \, Pr_G^{1.06} \, Y^{-1.83} \left(\frac{k_G}{d_i} \right) \qquad [19.4.6]$$

The homogeneous Reynolds number Re_H and the correction factor Y are calculated as follows when using this expression:

$$Re_H = \frac{\dot{m} d_i}{\mu_G} \left[x + \frac{\rho_G}{\rho_L} (1 - x) \right] \qquad [19.4.7]$$

$$Y = 1 - 0.1 \left[\left(\frac{\rho_L}{\rho_G} - 1 \right) (1 - x) \right]^{0.4} \qquad [19.4.8]$$

The heat transfer coefficient in the dryout region is calculated by a linear interpolation as before, but using the Cheng et al. (2008a) methods for x_{di} and x_{de} given earlier. If x_{di} or x_{de} is not defined at the mass velocity being considered (i.e. if it is calculated to be larger than 1.0), it is assumed to be equal to 0.999.

A heat transfer model for bubbly flow was added to the model for completeness sake. For this reason, the heat transfer coefficients in bubbly flow regime are calculated by the same method used for intermittent and slug flow. As for those flows, for bubbly flow the dryout angle θ_{dry} is set to zero. There were only about 20 data points in the bubbly flow regime and the current assumption works about as well as the method works for intermittent and slug flows.
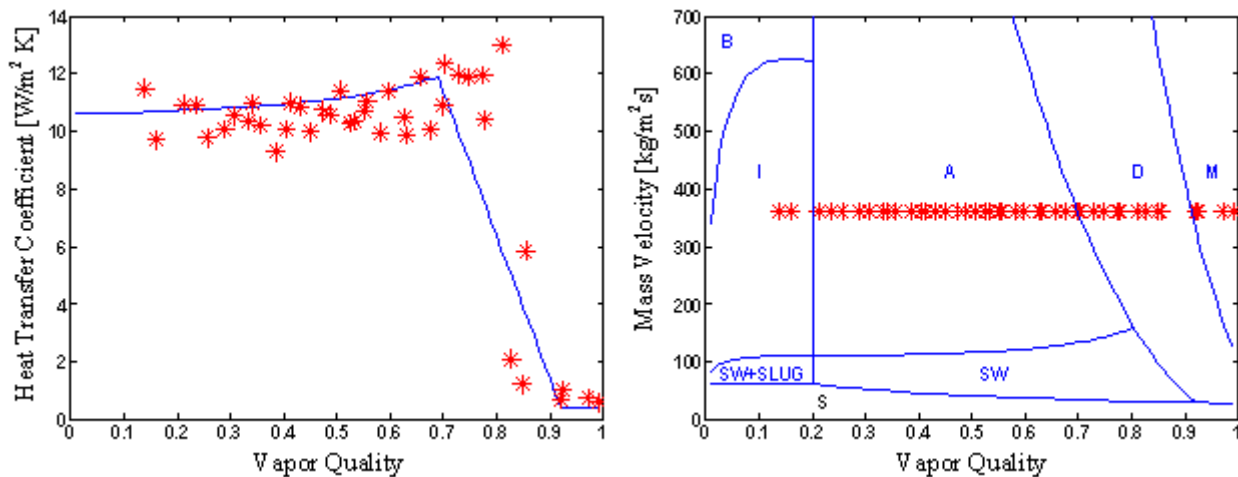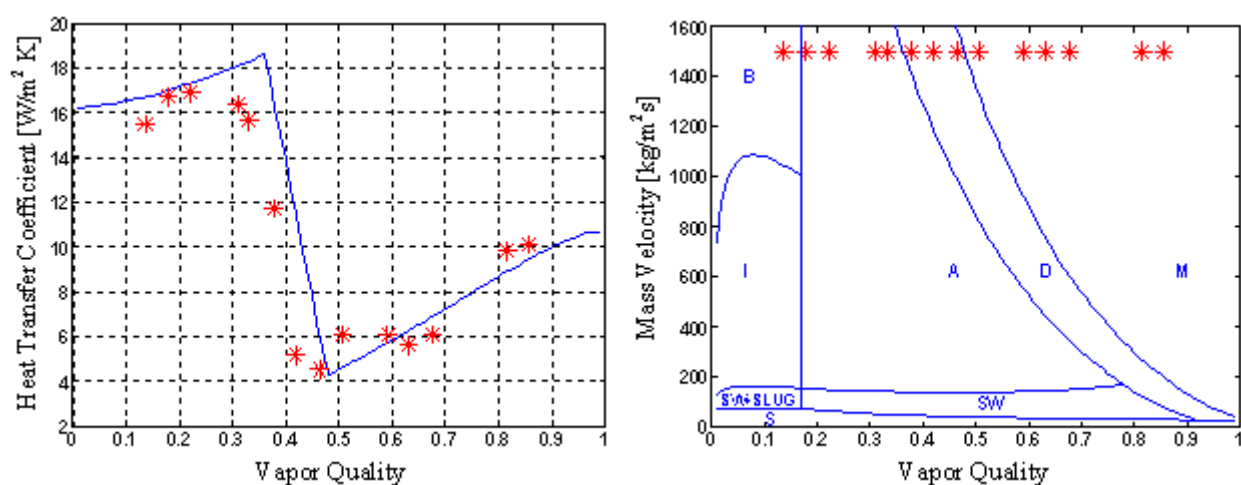

Figure 19.7. Flow boiling heat transfer coefficients predicted by Cheng et al. (2008a, 2008b). *Left*: **Predictions compared to the experimental data of Tanaka et al. (2001) for diameter of 1 mm, mass velocity of 360 kg/m²s, saturation temperature of 15 °C and heat flux of 9 kW/m²;** *Right*: **Predicted flow patterns corresponding to the experimental conditions of the heat transfer data points.**

Figure 19.7 shows a comparison of an experimental data set of Tanaka et al. (2001) for a diameter of 1 mm channel compared to the heat transfer model (left) and shows the individual test conditions of each data point plotted on the flow pattern map (right). This would approximately be within the operating range of an automotive air-conditioner for this size of channel. As can be seen, the predictions are quite good and capture the order of magnitude change in heat transfer coefficients with vapor quality. The onset of dryout is predicted to occur about 5-10% too early according to the heat transfer trends while the location of the beginning of mist flow seems to be captured well.

Figure 19.8 shows on the left a comparison of some data of Yun, Choi and Kim (2002) and Yun, Kim and Kim (2005) for a channel with a diameter of 2 mm at very high mass velocity. The conditions of each data point are plotted on the flow pattern map (right). This would approximately be within the upper design range of mass velocity for an automotive air-conditioner. As can be seen, the predictions are again quite good and capture the dramatic variation in heat transfer coefficients with vapor quality, although the onset of dryout and beginning of mist flow are each predicted to occur about 5% too late.

Figure 19.8. Flow boiling heat transfer coefficients predicted with the Cheng et al. (2008a, 2008b). *Left***: Predictions compared to the experimental data of Yun, Choi and Kim (2002) and Yun, Kim and Kim (2005) for diameter of 2 mm, mass velocity of 1500 kg/m2s, saturation temperature of 5 °C and heat flux of 30 kW/m^2;** *Right***: Predicted flow patterns corresponding to the experimental conditions of the heat transfer data points.**

Regarding the accuracy of the new Cheng et al. (2008b) heat transfer model compared to its database described above, 71% of the entire database was predicted within ±30% whilst 83% of the database without the dryout and mist flow data was captured within this range. On the other hand, only 48% of the mist flow data and 48% of the dryout regime data are captured within ±30%. The predictions for the dryout and mist flow regions are less accurate primarily due to the higher inaccuracy in such data (e.g. the very sharp downward slope in the dryout data with vapor quality means that a 2% error in the energy balance during a measurement has a huge effect when trying to predict those data), scatter in some data sets ranged up to ±40% and some very significant discrepancies were observed from one experimental study to another. Furthermore, as can be seen in Figures 19.7 and 19.8, the difficulties encountered in predicting the inception and completion of dryout in the flow pattern map to better than ±5% (which means some heat transfer data near these transitions are mistakenly identified to be in the nearby regime) can result in large heat transfer prediction errors near these boundaries. Thus, resolving these prediction errors for such data are not easy and these qualification comments should not be forgotten when measuring new CO_2 flow boiling data and when utilizing this model for comparison to new data and for design purposes. On the other hand, the sharp changes in heat transfer trends in CO_2 flow boiling data

when changing flow pattern are an excellent example of why flow pattern based prediction methods provide better reliability and accuracy than the old style methods that ignore flow pattern effects.

In summary, one unified approach for predicting (*i*) two-phase flow pattern transitions (with a diabatic map), (*ii*) two-phase frictional pressure drops and (*iii*) flow boiling heat transfer coefficients has been proposed and described above, i.e. the methods of Cheng et al. (2008a, 2008b). Additional accurate data and flow pattern observations are still required to make further future improvements.